Structural origin of deformation and dynamical heterogeneity in metallic glasses

Zeng-Yu Yang [1,2,3] and Lan-Hong Dai [1,2,4,*]

[1]State Key Laboratory of Nonlinear Mechanics, Institute of Mechanics, Chinese Academy of Sciences, Beijing 100190, China
[2]School of Engineering Science, University of Chinese Academy of Sciences, Beijing 100049, China
[3]Institute of Fluid Physics, China Academy of Engineering Physics, Mianyang, Sichuan 621900, China
[4]School of Future Technology, University of Chinese Academy of Sciences, Beijing 100049, China

(Received 29 June 2023; accepted 5 October 2023; published 3 November 2023)

Heterogeneity in the deformation field, especially in the form of shear bands, is a universal feature in disordered solids. The current paradigm presents the deformation heterogeneity as the result of structural inhomogeneity which is controlled by the concentration of atomic ordering clusters or flow defects. Here, we show that, in contrast to the population of atomic clusters, their topology, i.e., spatial distribution, is the root cause of the strain localization. This conclusion is reached via a decoupling tactic which completely eliminates the effect of concentration. Under loading stimuli, model glasses with identical concentration but various topological connectivity of atomic ordering clusters show remarkably distinct mechanical behaviors. Deformation heterogeneity and shear banding emergence are linked to glasses with strong topological connectivity. Topological connectivity can be not only characterized as the structural origin of strain localization, but is also transferable to detect the dynamical heterogeneity. These results are instrumental to rationalize the emergence of shear bands in disordered solids in terms of the pure structural information.

DOI: 10.1103/PhysRevMaterials.7.113601

I. INTRODUCTION

In the broad existed disordered packing media, deformation heterogeneity [1,2], for instance the directional percolation of localized strain to form shear bands [3–5], is ubiquitous and has been the object of tremendous experimental [6–8], computational [9–12], and theoretical [13–16] efforts over the last decades. Metallic glasses are not only of extensive application potential due to their outstanding mechanical behaviors [17], but also an ideal glass model for the investigation of the fundamental physics of the disordered materials. In metallic glasses, simulated evidences down to atomic scale have shown that the inherent inhomogeneous deformation and dynamical heterogeneity are dependent on both chemical composition [18,19] and cooling histories [20,21]. Since the fraction of atomic ordering clusters, e.g., icosahedron in CuZr system, also appear to vary with the evolution of deformation fields [22], the prevailing understanding underlying the inhomogeneous deformation field of metallic glasses is attributed it as the cause of the density of ordering clusters or flow defects [23–25]. For example, the key internal variables in the famous free-volume model [26] and shear transformation zone (STZ) framework [27,28] are the fraction of free volume and the number density of STZ, respectively. On the basis of this conception, the current approaches to achieve the ductility and homogeneous deformation in metallic glasses are based on rejuvenation process [29–31] which tailors the concentration of ordering or defect density via preloading [32,33], thermal process [34,35], and so on.

In spite of this, further experimental [36,37] and simulated [38,39] evidence were collected later on, revealing the profound effects of spatial connection of atomic ordering, namely, medium-range order [40,41], on the deformation behaviors of metallic glasses. For example, icosahedral clusters in CuZr systems exhibit strong spatial correlation and are prone to interpenetrate with each other [42], forming a percolating backbone. Such a spatial connection is validated to be closely related to the relaxation dynamics [43] and deformation heterogeneity [44]. These observations then provide a clear demonstration of the inherent structural inhomogeneity as well as another possible explanation to the physical origin of the deformation heterogeneity, being traced back to the spatial distribution, i.e., topology of atomic packing, rather than the purely statistic distribution or density.

Therefore, there is an emerging and imperative question: whether the fraction of ordering clusters or its topology is the root cause that leads to the inhomogeneity of deformation field in metallic glasses? Actually, this is a long-standing challenge due to the strong coupling between the fraction of atomic ordering and its spatial connection [20,45], thus leading to the determination of structural origin of deformation heterogeneity is still an open question.

In this work, we focus on this debate and provide a conclusive answer to this fundamental question, based on atomistic simulations and the decoupling strategy which completely eliminates the effect of fraction of ordering clusters. We are able to directly discuss the deformation behaviors of glass samples with identical fraction but distinct topology of atomic ordering. It is illustrated that such model glasses show various levels of deformation heterogeneity, ranging from homogeneous deformation to the formation of a shear band,

*lhdai@lnm.imech.ac.cn

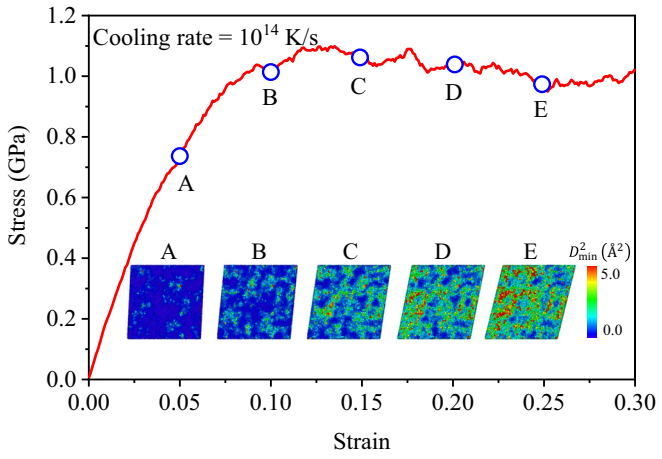

FIG. 1. Typical shear stress-strain curve of $Cu_{50}Zr_{50}$ metallic glass with fast cooling rate of 10^{14} K/s. The inset shows the evolution of spatial distribution of nonaffine displacement.

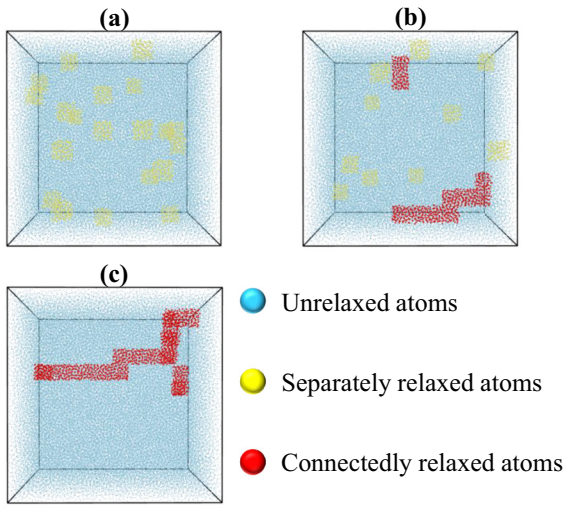

FIG. 2. Snapshots of $Cu_{50}Zr_{50}$ metallic glasses with connected factor equaling (a) 0.0, (b) 0.5, and (c) 1.0, respectively. Here, blue spheres denote atoms in the matrix. Yellow spheres denote separately distributed relaxed regions. Red spheres characterize relaxed atoms in connectedly relaxed regions.

suggesting the leading role of topology as the main driving factor for the strain localization leading to the emergence of shear band.

II. SIMULATION DETAILS

Here, atomistic simulations are carried out via the open source LAMMPS code [46]. The prototypical binary system $Cu_{50}Zr_{50}$ is used as the model glass. The embedded-atom potential provided by Mendelev *et al.* [47] is employed to describe the interatomic interactions. First of all, a soft $Cu_{50}Zr_{50}$ glass, containing 108 000 atoms is constructed by quenching the fully relaxed melting liquid (2050 K) into glassy state (50 K) with extremely fast cooling rate of 10^{14} K/ps. The obtained glass, with dimensions of $12.8 \times 12.8 \times 12.8$ nm^3, is then sheared along the *xy* direction and with strain rate of 10^8 s^{-1}. For the process of glass preparation and subsequent loading test, an *NPT* ensemble (constant number of atoms, constant pressure, and constant temperature) is utilized. Here, the pressure and temperature are controlled by using the Nose-Hoover thermostat [48]. The mechanical response is given in Fig. 1. It gives the evolution of spatial distribution of nonaffine displacement [28]. Intuitively, this glass sample shows the nearly homogeneous deformation field without the generation of strain localization or shear bands. This is in line with an earlier view that fast cooling rates will lead to rejuvenated glass states which are coupled with restrained shear banding instability [19,21].

Then, we insert additional structural inhomogeneity to this soft glass by further heating and relaxing a tiny fraction of atoms (nearly 2% of the total atoms). The selected regions, each with length scale of 1 nm in each direction, is relaxed at 850 K (slightly above the glass transition temperature) for 1 ns, namely, the relaxed region, while other atoms are simultaneously annealed at 50 K, referring to the matrix. In this relaxation process, the microcanonical ensemble (*NVE*) is utilized. To conduct model glasses with identical population but various topology of short-range order clusters, packing manners with different level of connectivity are carried out. As shown in Figs. 2(a) to 2(c), three typical model glasses with obviously distinct spatial distribution of relaxed regions are obtained. In Fig. 2(a), relaxed regions are distributed randomly and separately. In Fig. 2(b), half of the relaxed regions are connected. In contrast, the glass shown in Fig. 2(c) presents the fully connected network formed by relaxed regions. To quantify the level of connectivity and distinguish the topology of ordering clusters in these three model glasses, the connected factor χ_{con} is defined as the fraction of connected regions in all relaxed regions. In this connection, the model glasses in Figs. 2(a) to 2(c) correspond to $\chi_{con} = 0.0$, $\chi_{con} = 0.5$, and $\chi_{con} = 1.0$, respectively. There is general consensus that anisotropic structures, acting as the intrinsic feature, play an important role on the mechanical behavior of metallic glasses [49–51]. Thus, the relaxed regions as shown in Figs. 2(b) and 2(c) are mainly connected along a certain direction, for the sake of remodeling the intrinsic anisotropic effect in metallic glasses. It is noted that periodic boundary conditions along the *x*, *y*, and *z* directions are imposed for all the simulations. The time step is set to be 0.002 ps.

III. RESULTS AND DISCUSSIONS

A. Decoupling between population and topology of structural ordering

It is generally accepted that glass samples will become more stable after relaxing at temperature near the glass transition [52,53]. Therefore, it is expected that the heating and subsequent relaxing process mentioned in Sec. II is able to drive the glass states towards being less energetic. This can be clarified by the comparison of the level of potential energy in both the matrix and the relaxed regions as shown in Figs. 3(a) and 3(b). It is observed that the relaxed regions show less potential energy than the matrix. It indicates that atoms in the relaxed regions are much more stable than those in the matrix. This phenomenon is suitable for both Cu and

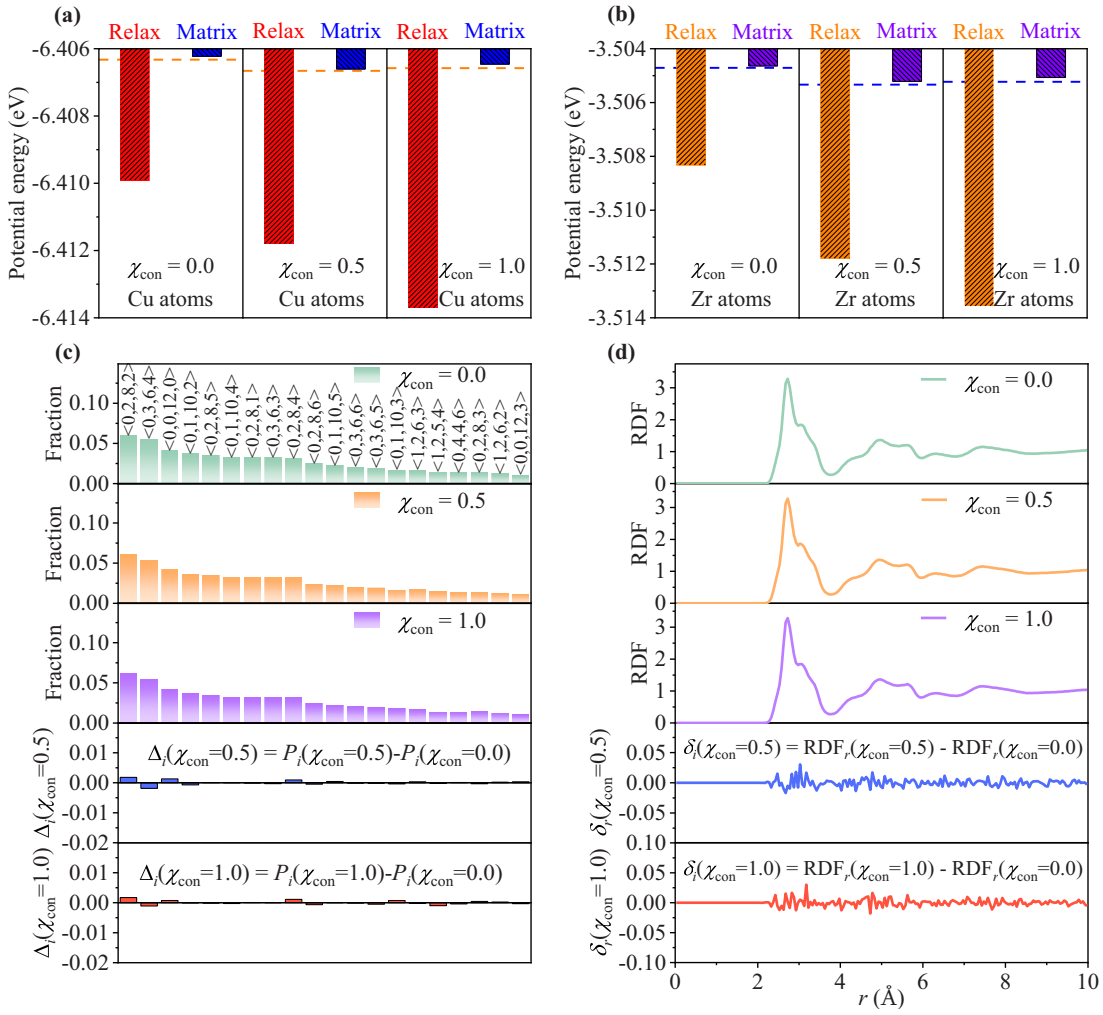

FIG. 3. (a) The per atom potential energy for Cu atoms in various sample glasses. (b) The per atom potential energy for Zr atoms in various sample glasses. (c) Statistic distributions of static short-range structures. First to third rows: Distribution of 20 most frequent Voronoi clusters in samples with $\chi_{con} = 0.0$, $\chi_{con} = 0.5$, and $\chi_{con} = 1.0$, respectively. Fourth to fifth rows: Deviations among the three sample glasses in the distribution of Voronoi polyhedra. (d) Statistically structural information via radial distribution functions. First to third rows: Radial distribution functions for $Cu_{50}Zr_{50}$ metallic glasses with $\chi_{con} = 0.0$, $\chi_{con} = 0.5$, and $\chi_{con} = 1.0$, respectively. Fourth to fifth rows: Deviations among the three sample glasses in radial distribution functions.

Zr atoms. In addition, it is intriguing to find that the energy reduction is enhanced as χ_{con} increases from 0.0 to 1.0. This gives the intuitive evidences that the topology, specifically, the connectivity, of stable regions is critical for the energetic state. Moreover, since the relaxing procedure is carried out on a tiny fraction of atoms, it would not induce a noticeable difference on the overall energy states, as shown by the dashed lines in Figs. 3(a) and 3(b). Here, only subtle fluctuations of the overall energy states are observed among glasses with different χ_{con} values. It indicates that the structural topology can be tailored by the premise of not affecting the overall energy state.

We then test the effect of decoupling between population and topology. On the one hand, the statistic distribution of short-range order clusters is investigated. Figure 3(c) shows the Voronoi polyhedra analysis for glasses with various topology, as evaluated by the connected factor χ_{con}. Here, the label of Fig. 3(c) is the Voronoi index, which has the form of $\langle n_3, n_4, n_5, n_6 \rangle$. Here, n_i denotes the number of i-edge polygons. The Voronoi index is able to identify the Voronoi structure and is widely used to characterize the short-range atomic packings [41,54]. It is clearly seen that these three samples show almost the same fraction on each type of Voronoi clusters. This is further quantitatively validated by the fourth and fifth rows of Fig. 3(c). It can be seen that the deviation Δ_i is approaching zero. Such a similarity on the statistically structural features can also be identified by the almost identical total radial distribution functions (RDFs) among these three model glasses, as seen in Fig. 3(d). On the other hand, the topology or spatially packing manner of short-range order clusters is uncovered by monitoring the connectivity of full icosahedron in glasses with various χ_{con}. Here, two full icosahedral clusters are connected if they share atoms. We characterize all of the icosahedral clusters and identify the details that they interpenetrate with each other and thus form the bigger network. Consequently, all of the

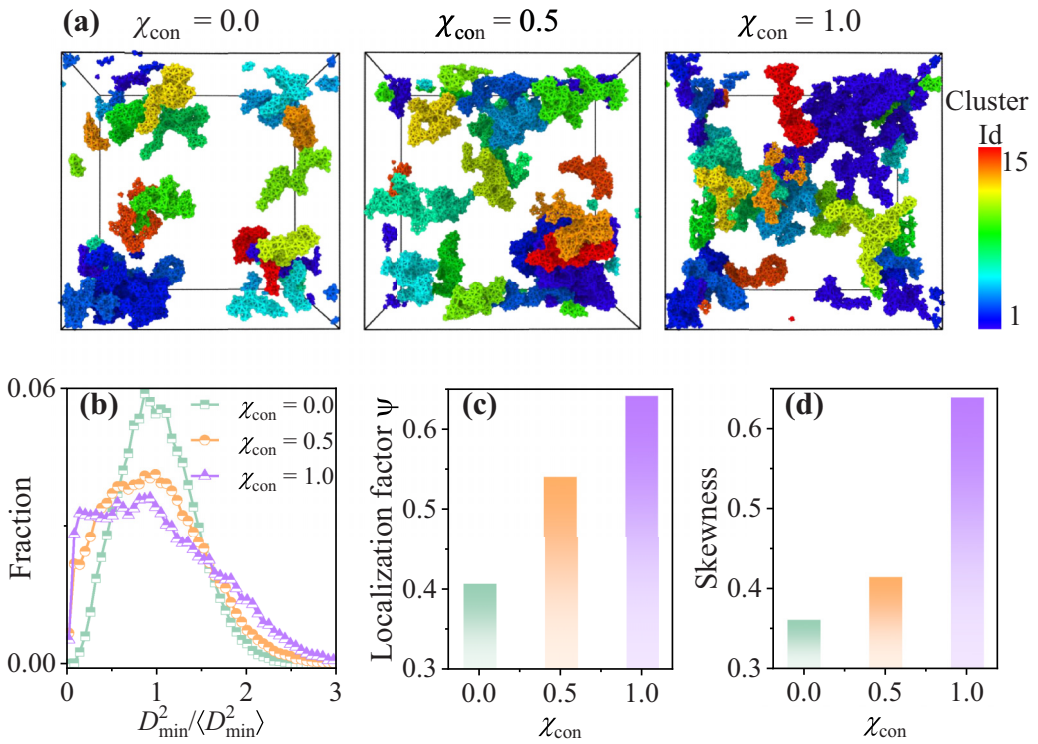

FIG. 4. (a) The spatial distribution of interpenetrating full icosahedral clusters for samples with different χ_{con} values. The 15 largest clusters are visualized with atoms color-coded according to the cluster id. (b) Statistical distribution of reduced non-affine displacement $D^2_{min}/\langle D^2_{min}\rangle$ at strain of 0.30. (c) The localization factor Ψ of strain field. (d) The skewness of strain field.

interpenetrating clusters are obtained and then sorted in order according to the number of their containing atoms. Figure 4(a) shows the spatial distribution of the top 15 interpenetrating clusters. It is seen that full icosahedral clusters are prone to connect with each other in glasses with high χ_{con} values, leading to the huge structural network. Such a structural network might act as the stiff backbone to resist deformation under external stimuli. In this connection, this gives the direct evidence that our decoupling strategy eliminates the population factor and is able to purely concentrate on the effect of topology on strain localization behavior.

B. Topological packing of ordering structure controls the deformation inhomogeneity

Having singled out the topological features from the structural information, the next task is to figure out its critical role on the deformation inhomogeneity. First of all, the strain localization behavior is briefly unveiled by the distribution of reduced non-affine displacement $D^2_{min}/\langle D^2_{min}\rangle$ [28], as shown in Fig. 4(b). It is seen that glass with $\chi_{con} = 0.0$ exhibits nearly a Gaussian distribution, indicating a uniform-like deformation field. In contrast, the distribution of $D^2_{min}/\langle D^2_{min}\rangle$ in glasses with $\chi_{con} = 0.5$ and $\chi_{con} = 1.0$ show visible non-Gaussian tails, indicating the pronounced deformation inhomogeneity. To intuitively and quantitatively evaluate the degree of deformation localization, two parameters, namely, the localization factor and skewness are introduced [21]. Here, the localization factor Ψ is defined as

$$\Psi = \sqrt{\frac{1}{N}\sum_i \left(\frac{\alpha_i}{\langle\alpha_i\rangle} - 1\right)^2}, \tag{1}$$

and the parameter skewness S_k has the form of

$$S_k = \left\langle \left(\frac{\alpha_i - \langle\alpha_i\rangle}{\sigma}\right)^3 \right\rangle. \tag{2}$$

Here, α_i represents the physical entity α for atom i and can be replaced by $D^2_{min}/\langle D^2_{min}\rangle$ in this work. N denotes the total number of atoms and σ demonstrates the standard deviation of $D^2_{min}/\langle D^2_{min}\rangle$. $\langle\cdots\rangle$ denotes the statistical average. More details about these two parameters can be found in Ref [21]. The results are shown in Figs. 4(c) and 4(d). It is intuitive that the strain localization and anisotropic manner of the deformation field are enhanced with the increasing values of χ_{con} as well as the more remarkable anisotropic effect of structural packing manners shown in Fig. 2. Since we eliminated the effect of population of atomic ordering, it is suggested that the structural origin of deformation heterogeneity is radically the topological packing.

We also calculate the atomic effective strain $\widetilde{\Lambda}$ based on the recently developed two-term gradient (TTG) model [12]. In contrast to the nonaffine displacement, $\widetilde{\Lambda}$ covers both the affine and nonaffine components of deformation. Figure 5(a) presents the evolution of spatial distribution of $\widetilde{\Lambda}$ in the three glasses under shear loading. Intuitively, in glass with $\chi_{con} = 1.0$, plastic regions with high $\widetilde{\Lambda}$ are gradually aggregating along the shear direction, causing the emergence of a shear band. For comparison, plastic units are activated randomly and homogeneously in glass with no connected relaxed regions ($\chi_{con} = 0.0$). Figure 5(b) shows the evolution of the effective strain in both the strain-localized region and the matrix during deformation. Strain localization pops up at

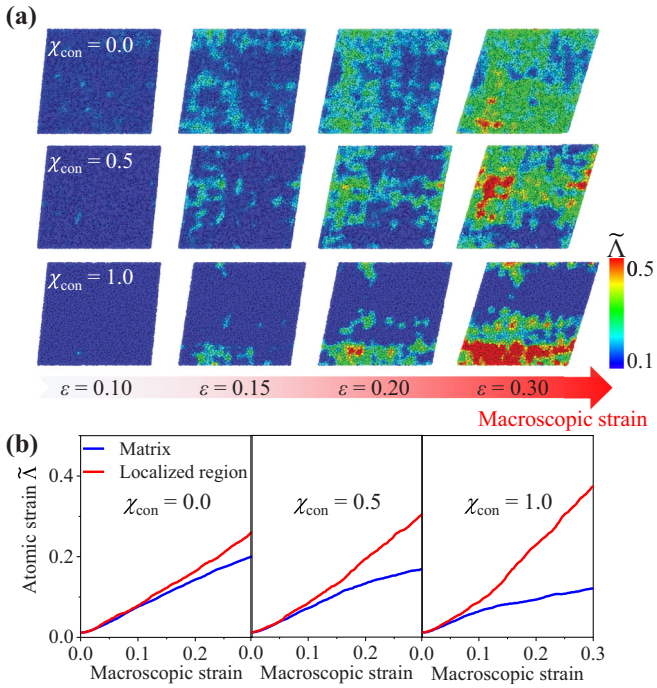

FIG. 5. (a) Spatial distributions of effective strain at various applied strains. (b) Evolution of effective atomic strain for samples with $\chi_{con} = 0.0$, $\chi_{con} = 0.5$, and $\chi_{con} = 1.0$, respectively.

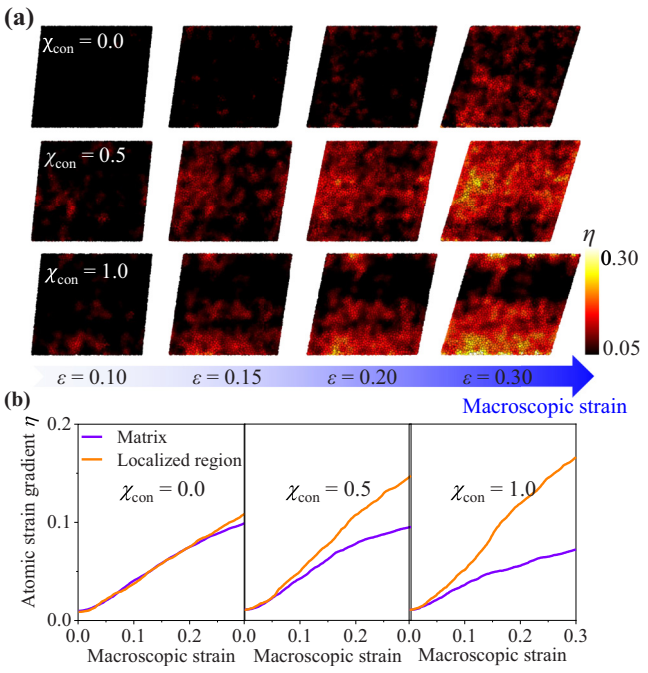

FIG. 6. (a) Spatial distributions of effective strain gradient at various applied strains. (b) Evolution of effective atomic strain gradient for samples with $\chi_{con} = 0.0$, $\chi_{con} = 0.5$, and $\chi_{con} = 1.0$, respectively.

the point when atomic strain in localized region deviates from the matrix level. Intuitively, the deformation inhomogeneity in glass with $\chi_{con} = 1.0$ occurs indeed prior to that in glass with $\chi_{con} = 0.5$, followed by the case with $\chi_{con} = 0.0$. In addition, the mismatch between the matrix and the localized region is more pronounced with the increasing χ_{con}, leading to the strong aggregation of plastic deformation as well as the subsequent onset of shear band in glass with $\chi_{con} = 1.0$.

Since the strain gradient is the direct reflection of deformation inhomogeneity and is also the driving force of the emergence of shear bands [55–57], we also calculate the effective strain gradient η at atomic scale based on the TTG [12]. First of all, the projected strain gradient fields color coded by η at various applied strains are shown in Fig. 6(a). It is clearly seen that the glass sample with the highest level of connectivity of short-range order clusters shows the most pronounced strain-gradient effect while the sample where the relaxed regions are not connected does not exhibit visible strain gradient. This is quantitatively validated by Fig. 6(b) which plots the evolution of atomic strain gradient in both the matrix and the localized region. As shown in Fig. 6(b), the strain-gradient effect is magnified step by step, especially in the shear band region of the glass with $\chi_{con} = 1.0$. Moreover, the high strain-gradient region perfectly overlaps with the shear band in the glass with $\chi_{con} = 1.0$. This stresses the critical role of the strain gradient in shear banding emergence.

In addition, comparing Figs. 2, 4(a), 5(a), as well as 6(a), it is intriguing to find that interpenetrating full icosahedral clusters are prone to generate in connected relaxed regions, as evidenced by the correspondence between red regions in Fig. 2 and the blue clusters shown in Fig. 4(a). Such regions, in turn, form stiff backbones, leading to the high activation barriers and low attendance of shear transformation, as evidenced by the fields of strain and strain gradient shown in Figs. 5(a) and 6(a), respectively. This is probably the root cause of the topology of short-range order clusters playing a significant role on the deformation behavior in metallic glasses.

To validate the spatial correspondence between the structural signature evaluated by interpenetrating full icosahedral clusters and the deformation field, additional glass samples with $\chi_{con} = 0.7$, $\chi_{con} = 0.8$, and $\chi_{con} = 0.9$ are prepared, as shown in Fig. 7. Similar characterizations of the interpenetrating network of full icosahedral clusters are carried out, as shown in the second row of Fig. 7. Also, we cast shear loading tests with identical settings on these glass samples. The deformation field is demonstrated via nonaffine displacement, as shown in the third row of Fig. 7. These observations show that regions lack of interpenetrating full icosahedral clusters overlap with regions where strong localization of strain occurs. This indicates the critical role of topology acting as the structural carriers of deformation inhomogeneity.

More evidence to depict the critical role of initially structural topology on deformation inhomogeneity is needed in light of the percolation process of STZ spanning to large scales in the form of shear band. Here, an atom with $\tilde{\Lambda}$ beyond 0.25 is characterized as being part of the plastic regions. We calculate the linkage among plastic atoms and characterize the size of all of the percolated plastic regions. S_{all} denotes the total number of plastic atoms and S_{max} refers to the size of the largest percolating region. First of all, we monitor the percolation process of STZs by investigating the time evolution of S_{max} for the three model glass. As shown

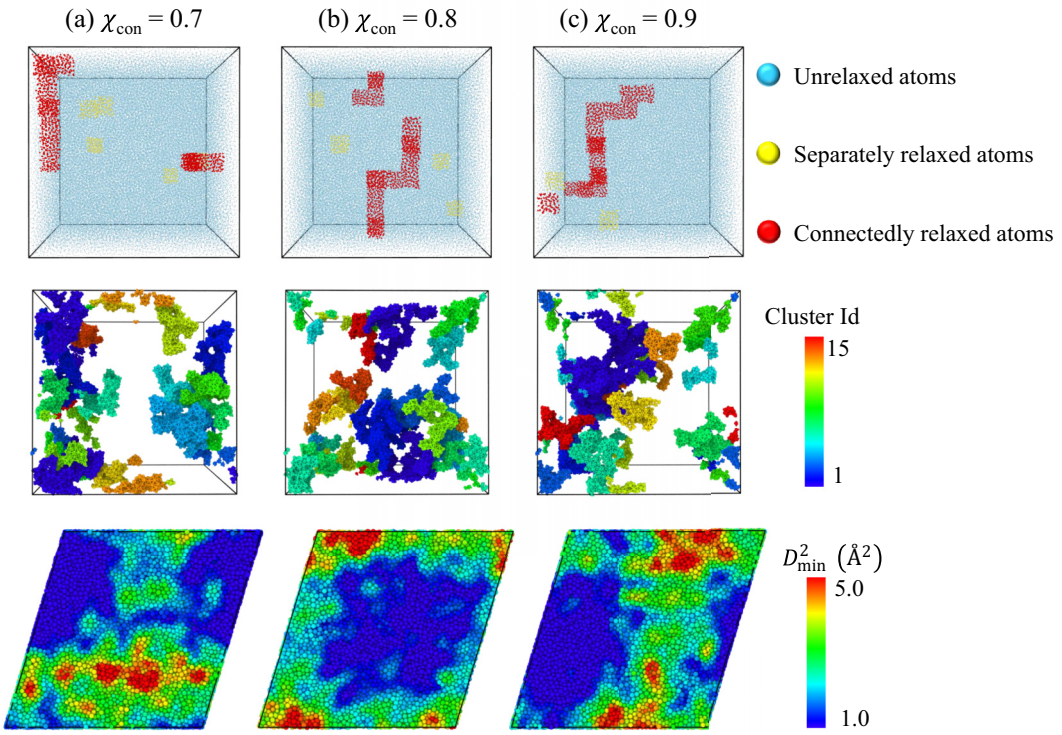

FIG. 7. Spatial correspondence among distribution of relaxed regions, distribution of full icosahedral clusters, and strain field in sample glasses with (a) $\chi_{con} = 0.7$, (b) $\chi_{con} = 0.8$, and (c) $\chi_{con} = 0.9$, respectively.

in Fig. 8(a), S_{max} displays the drastic rise in the glass with strongest connectivity of full icosahedral clusters while only a weak increment is observed in glass with $\chi_{con} = 0.0$. During the deformation of disordered solids, the two processes of percolation of coexisted STZ and the activation of new STZ are inherently coupled. Their competition is the principal source of the strain field being localized or homogeneous. To carefully demonstrate this competing behavior, the dimensionless percolating factor, i.e., S_{max}/S_{all} is introduced [12]. It is noted that the abrupt increase in S_{max}/S_{all} means the more pronounced growth of S_{max} than S_{all}, indicating that the percolation of plastic atoms is dominant over the stochastic activation process. In this sense, it is the significant signature of strain aggregation and the onset of the shear band. Figure 8(b) shows the time evolution of S_{max}/S_{all} for the three model glasses. As is expected, the occurrence of percolating events is captured in glass with $\chi_{con} = 0.5$ and $\chi_{con} = 1.0$. In contrast, the evolution of S_{max}/S_{all} in glass with $\chi_{con} = 0.0$ is fairly stable without any evident increment. This reflects the sluggish percolating process which leads to the homogenous deformation field as seen in Fig. 5(a).

The deformation response is further demonstrated by tracing the evolution of possible elemental atomic-scale motions, i.e., shear, dilatation and rotation. In Ref. [12], these three highly entangled motions were decoupled from the deformation field and parameters ξ_S, ξ_D, and ξ_R were used to quantify the atomic-scale shear, dilatation, and rotation motions, respectively. Here, ξ_S, ξ_D, and ξ_R for each atom in the three

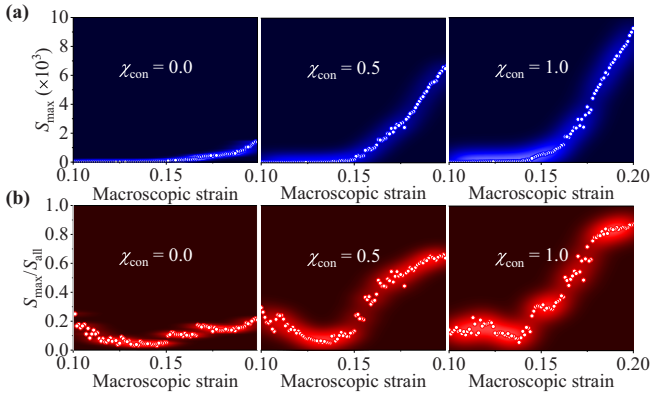

FIG. 8. (a) Size of the maximum percolating cluster with plastic atoms interpenetrating each other as a function of applied strain. (b) Time evolution of percolating factor S_{max}/S_{all} during loading.

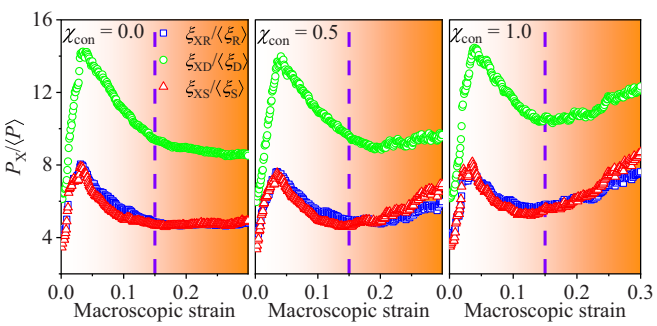

FIG. 9. Extreme value analysis showing the evolution of normalized extreme values, $\xi_{XR}/\langle \xi_R \rangle$, $\xi_{XD}/\langle \xi_D \rangle$, $\xi_{XS}/\langle \xi_S \rangle$, for rotation, dilatation, and shear, respectively.

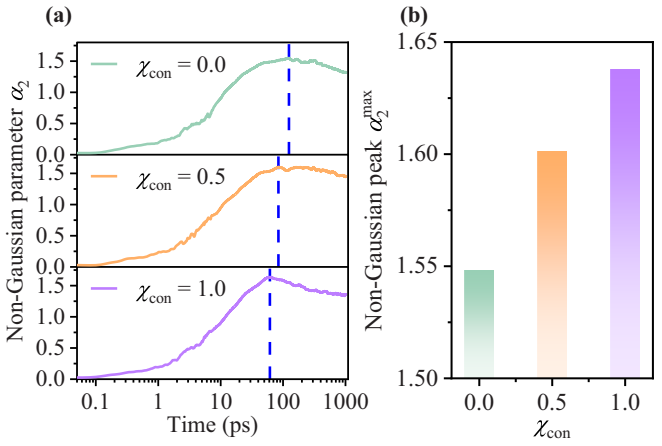

FIG. 10. Transferability of χ_{con} in correlating dynamic inhomogeneity of metallic glasses. (a) Evolution of non-Gaussian parameters during relaxation process for glass samples with various χ_{con} values. (b) Maximum non-Gaussian parameters for samples with various values of χ_{con}.

model glasses are calculated. Since the distributions of ξ_S, ξ_D, and ξ_R are proved to display an inherent non-Gaussian manner with long tails being the reflection of the inhomogeneity [12], here the extreme value analysis is used to track the extreme sites residing in the long tail. Atoms with the top 1% values of parameter P are picked out. P can be replaced by ξ_S, ξ_D, and ξ_R. Then the reduced extreme value $P_X/\langle P\rangle$, where P_X denotes the mean value of the selected atoms and $\langle P\rangle$ denotes the mean value in the overall sample is calculated. The evolution of $\xi_{XR}/\langle\xi_R\rangle$, $\xi_{XD}/\langle\xi_D\rangle$, $\xi_{XS}/\langle\xi_S\rangle$ for the three model glasses are shown in Fig. 9. The observed higher level of $\xi_{XD}/\langle\xi_D\rangle$ over that of $\xi_{XR}/\langle\xi_R\rangle$ and $\xi_{XS}/\langle\xi_S\rangle$ indicates that the dilatation localization is the dominant mode in the deformation inhomogeneity. This is in concert with the previous simulated and experimental works [12,58]. In addition, the three tested glasses also show various evolving manners of $P_X/\langle P\rangle$. With the increasing of χ_{con}, there is a more pronounced growing trend of $P_X/\langle P\rangle$ in the regime where applied strain exceeds 0.15. Since $P_X/\langle P\rangle$ can quantify the localization behavior of the extreme sites, such an increment in $P_X/\langle P\rangle$ suggests the growing the strain localization is related to samples with higher connectivity.

C. Topological packing of ordering structure controls the dynamical heterogeneity

In addition to the deformation inhomogeneity, we also test the transferability of χ_{con} in correlating the dynamical heterogeneity. To address this issue, the glass samples are relaxed at 300 K for 1 ns. The non-Gaussian parameter α_2, which is commonly used to measure the dynamical heterogeneity of a disordered system [59], is then calculated. The evolution of α_2 for glasses with various χ_{con} is monitored, as shown in Fig. 10(a). Generally, the peak value α_{max}^2 is the signature of the degree of dynamic heterogeneity. As seen in Fig. 10(b), the growing of topological connectivity is accompanied by the rise of α_{max}^2, indicating an increasing dynamic heterogeneity. This phenomenon suggests that the structural topology proves highly versatile in being able to correlate dynamic heterogeneity.

IV. CONCLUSION

In summary, we presented a series of detailed quantitative characterizations of atomic structure and deformation field in model glasses with an identical fraction but various spatial topologies of atomic orderings. In contradiction with the prevailing dominant paradigm that deems deformation heterogeneity induced solely by density of atomic ordering or flow defects, we demonstrated quantitatively that their topology, e.g., spatial connection, plays a crucial role. Acting as the root cause of strain localization, structural topology is strongly related to the process of shear banding emergence. Such a structure-property correlation is also validated in determining the dynamical heterogeneity. In addition, it is observed that the inherent dynamical heterogeneity is also controlled by the topology of atomic ordering. Moreover, it is suggested that distinct deformation heterogeneity can be achieved without influencing the overall energy state. This provides an alternative understanding of structural rejuvenation which may not be completely related to high energy. The emerging picture of breaking the spatial connection of atomic ordering but keeping its fraction opens up plenty of opportunities for the material discovery of metallic glasses with improving plasticity and unaffected strength.

ACKNOWLEDGMENTS

This work is financially supported by the NSFC Basic Science Center Program for "Multiscale Problems in Nolinear Mechanics" (Grant No. 11988102), the Strategic Priority Research Program (Grants No. XDB22040302 and No. XDB22040303), and the Key Research Program of Frontier Sciences (Grant No. QYZDJSSWJSC011). This work is also supported by Ye Qisun Science Foundation of National Natural Science Foundation of China (Grant No. U2141204) and the Opening Project of State Key Laboratory of Explosion Science and Technology (Beijing Institute of Technology, Grant No. KFJJ23-03M).

[1] M. L. Falk and J. Langer, Annu. Rev. Condens. Matter Phys. **2**, 353 (2011).
[2] A. Nicolas, E. E. Ferrero, K. Martens, and J.-L. Barrat, Rev. Mod. Phys. **90**, 045006 (2018).
[3] A. Greer, Y. Cheng, and E. Ma, Mater. Sci. Eng.: R **74**, 71 (2013).
[4] *Adiabatic Shear Localization*, 2nd ed., edited by B. Dodd and Y. Bai (Elsevier, Oxford, 2012).

[5] T. C. Hufnagel, C. A. Schuh, and M. L. Falk, Acta Mater. **109**, 375 (2016).

[6] Y. H. Liu, D. Wang, K. Nakajima, W. Zhang, A. Hirata, T. Nishi, A. Inoue, and M. W. Chen, Phys. Rev. Lett. **106**, 125504 (2011).

[7] V. Schmidt, H. Rösner, M. Peterlechner, G. Wilde, and P. M. Voyles, Phys. Rev. Lett. **115**, 035501 (2015).

[8] V. Hieronymus-Schmidt, H. Rösner, G. Wilde, and A. Zaccone, Phys. Rev. B **95**, 134111 (2017).

[9] D. Richard, M. Ozawa, S. Patinet, E. Stanifer, B. Shang, S. A. Ridout, B. Xu, G. Zhang, P. K. Morse, J.-L. Barrat, L. Berthier, M. L. Falk, P. Guan, A. J. Liu, K. Martens, S. Sastry, D. Vandembroucq, E. Lerner, and M. L. Manning, Phys. Rev. Mater. **4**, 113609 (2020).

[10] Y. C. Hu, P. F. Guan, M. Z. Li, C. T. Liu, Y. Yang, H. Y. Bai, and W. H. Wang, Phys. Rev. B **93**, 214202 (2016).

[11] P. Cao, M. P. Short, and S. Yip, Proc. Natl. Acad. Sci. USA **116**, 18790 (2019).

[12] Z. Y. Yang, Y.-J. Wang, and L.-H. Dai, Phys. Rev. Res. **4**, 023220 (2022).

[13] A. Lemaître, Phys. Rev. Lett. **89**, 195503 (2002).

[14] M. Jiang and L. Dai, J. Mech. Phys. Solids **57**, 1267 (2009).

[15] M. L. Manning, E. G. Daub, J. S. Langer, and J. M. Carlson, Phys. Rev. E **79**, 016110 (2009).

[16] A. Furukawa and H. Tanaka, Nat. Mater. **8**, 601 (2009).

[17] C. A. Schuh, T. C. Hufnagel, and U. Ramamurty, Acta Mater. **55**, 4067 (2007).

[18] Y. Cheng, A. Cao, H. Sheng, and E. Ma, Acta Mater. **56**, 5263 (2008).

[19] Z. Y. Yang, Y. J. Wang, and L. H. Dai, Scr. Mater. **162**, 141 (2019).

[20] Y. Q. Cheng, E. Ma, and H. W. Sheng, Phys. Rev. Lett. **102**, 245501 (2009).

[21] Z. Y. Yang and L. H. Dai, Phys. Rev. Mater. **5**, 123602 (2021).

[22] A. J. Cao, Y. Q. Cheng, and E. Ma, Acta Mater. **57**, 5146 (2009).

[23] Z. D. Sha, Y. P. Feng, and Y. Li, Appl. Phys. Lett. **96**, 061903 (2010).

[24] J. Ding, Y. Q. Cheng, and E. Ma, Appl. Phys. Lett. **101**, 121917 (2012).

[25] E. Ma and J. Ding, Mater. Today **19**, 568 (2016).

[26] F. Spaepen, Acta Metall. **25**, 407 (1977).

[27] A. S. Argon, Acta Metall. **27**, 47 (1979).

[28] M. L. Falk and J. S. Langer, Phys. Rev. E **57**, 7192 (1998).

[29] Y. Sun, A. Concustell, and A. L. Greer, Nat. Rev. Mater. **1**, 16039 (2016).

[30] J. Pan, Y. X. Wang, Q. Guo, D. Zhang, A. L. Greer, and Y. Li, Nat. Commun. **9**, 560 (2018).

[31] A. Barbot, M. Lerbinger, A. Lemaître, D. Vandembroucq, and S. Patinet, Phys. Rev. E **101**, 033001 (2020).

[32] Y. Zhang, W. H. Wang, and A. L. Greer, Nat. Mater. **5**, 857 (2006).

[33] F. Meng, K. Tsuchiya, Seiichiro II, and Y. Yokoyama, Appl. Phys. Lett. **101**, 121914 (2012).

[34] S. V. Ketov, Y. H. Sun, S. Nachum, Z. Lu, A. Checchi, A. R. Beraldin, H. Y. Bai, W. H. Wang, D. V. Louzguine-Luzgin, M. A. Carpenter, and A. L. Greer, Nature (London) **524**, 200 (2015).

[35] J. Saida, R. Yamada, M. Wakeda, and S. Ogata, Sci. Technol. Adv. Mater. **18**, 152 (2017).

[36] T. Fujita, K. Konno, W. Zhang, V. Kumar, M. Matsuura, A. Inoue, T. Sakurai, and M. W. Chen, Phys. Rev. Lett. **103**, 075502 (2009).

[37] S. Hilke, H. Rösner, D. Geissler, A. Gebert, M. Peterlechner, and G. Wilde, Acta Mater. **171**, 275 (2019).

[38] P. Zhao, J. Li, J. Hwang, and Y. Wang, Acta Mater. **134**, 104 (2017).

[39] Z. Y. Yang and L. H. Dai, Phys. Rev. Mater. **6**, L100602 (2022).

[40] D. B. Miracle, Nat. Mater. **3**, 697 (2004).

[41] H. W. Sheng, W. K. Luo, F. M. Alamgir, J. M. Bai, and E. Ma, Nature (London) **439**, 419 (2006).

[42] M. Li, C. Z. Wang, S. G. Hao, M. J. Kramer, and K. M. Ho, Phys. Rev. B **80**, 184201 (2009).

[43] Z. W. Wu, W. Kob, W.-H. Wang, and L. Xu, Nat. Commun. **9**, 5334 (2018).

[44] M. Lee, C. M. Lee, K. R. Lee, E. Ma, and J. C. Lee, Acta Mater. **59**, 159 (2011).

[45] J. Ding, Y. Q. Cheng, and E. Ma, Acta Mater. **69**, 343 (2014).

[46] S. Plimpton, J. Comput. Phys. **117**, 1 (1995).

[47] M. I. Mendelev, Y. Sun, F. Zhang, C. Z. Wang, and K. M. Ho, J. Chem. Phys. **151**, 214502 (2019).

[48] S. Nosé, J. Chem. Phys. **81**, 511 (1984).

[49] W. Dmowski, T. Iwashita, C.-P. Chuang, J. Almer, and T. Egami, Phys. Rev. Lett. **105**, 205502 (2010).

[50] S. Cui, H. Liu, and H. Peng, Phys. Rev. E **106**, 014607 (2022).

[51] H. Wang, W. Dmowski, Y. Tong, Z. Wang, Y. Yokoyama, J. Ketkaew, J. Schroers, and T. Egami, Phys. Rev. Lett. **128**, 155501 (2022).

[52] A. Slipenyuk and J. Eckert, Scr. Mater. **50**, 39 (2004).

[53] R. Raghavan, P. Murali, and U. Ramamurty, Metall. Mater. Trans. A **39**, 1573 (2008).

[54] Y. Wu, D. Cao, Y. Yao, G. Zhang, J. Wang, L. Liu, F. Li, H. Fan, X. Liu, H. Wang, X. Wang, H. Zhu, S. Jiang, P. Kontis, D. Raabe, B. Gault, and Z. Lu, Nat. Commun. **12**, 6582 (2021).

[55] Z. L. Tian, Y. J. Wang, Y. Chen, and L. H. Dai, Phys. Rev. B **96**, 094103 (2017).

[56] N. Yan, Z. Li, Y. Xu, and M. A. Meyers, Prog. Mater. Sci. **119**, 100755 (2021).

[57] L. Q. Shen, P. Luo, Y. C. Hu, H. Y. Bai, Y. H. Sun, B. A. Sun, Y. H. Liu, and W. H. Wang, Nat. Commun. **9**, 4414 (2018).

[58] S. Kang, D. Wang, A. Caron, C. Minnert, K. Durst, C. Kübel, and X. Mu, Adv. Mater. **35**, 2212086 (2023).

[59] N. P. Walter, A. Jaiswal, Z. Cai, and Y. Zhang, Comput. Phys. Commun. **228**, 209 (2018).